JOURNAL OF CATALYSIS **161,** 667–686 (1996)
ARTICLE NO. 0229

Multicomponent Thin Film Molybdate Catalysts for the Selective Oxidation of 1,3-Butadiene

Joe Zou and Glenn L. Schrader[1]

Department of Chemical Engineering, Center for Interfacial Materials and Crystallization, and Ames Laboratory—USDOE at Iowa State University, Ames, Iowa 50011

Received October 26, 1995; revised February 23, 1996; accepted March 12, 1996

The selective oxidation of 1,3-butadiene was examined over single and multiphase $NiMoO_4$–MoO_3 thin film catalysts prepared by reactive sputtering. Previous studies of precipitated catalysts have indicated that synergism occurs for these multicomponent materials: sputtered films behaved similarly but tended to be more active and selective. XRD, LRS, XRF, XPS, SEM, and TEM were used to characterize the α-MoO_3 and α-$NiMoO_4$ thin films; for most bilayer materials, an additional phase, β-$NiMoO_4$, was present in an interfacial region. Selectivity for furan, 2(5*H*)-furanone, and maleic anhydride was enhanced by the preparation of the materials as layered films.

1. INTRODUCTION

Multicomponent metal oxides are widely used in industrial selective oxidation catalysis: for example, molybdate catalysts for the ammoxidation of propylene involve many components and phases (1–4). Despite the considerable advances in the understanding of the mechanism of selective oxidation catalysis for single-phase materials, there is a need to improve our understanding of the nature of catalysis by complex multiphase oxides. This is motivated in part by the enhancement in activity and selectivity typically associated with multicomponent catalysts. However, the nature of the interaction between the phases may be quite variable for different combinations of metal oxides: differences in composition and structure can result in the formation of solid solutions, epitaxial layers, defect boundaries, new interfacial materials, etc. In addition, catalysts prepared by conventional techniques (such as precipitation) may have complex morphologies and numerous contacting arrangements. In general there is a need for more definitive characterization of multicomponent catalysts and for further investigation of the compositional and structural relationships to catalytic activity.

Several general approaches which have been undertaken to determine the nature of multicomponent catalysts used in selective oxidation (5). Coherent phase boundaries were proposed to occur for V_2O_5–TiO_2 catalysts based on a crystallographic model for the contact between specific crystal planes (6–8). Transmission electron microscopy was used to examine the interface, but the sample was observed to be reactive in the electron beam. Only limited information about the structure and composition at the interface could be obtained. It was also suggested that microdomains due to specific preparation methods or "sample history" may modify the interfaces (5). Coherent intergrowth domains may also be formed during catalytic operation as proposed for VPO materials (9).

The concept of coherent interfaces was extended to other multicomponent systems such as $CoMoO_4$, MoO_3, and TiO_2 (10). In these studies, it was determined that the crystallographic misfit was less than 10% between the (100) $CoMoO_4$ and (010) MoO_3 cleavage planes. However, direct experimental evidence of this crystallographic match was difficult to obtain. Enhancement in catalytic activity for the conversion of butane to maleic anhydride was explained in terms of increased oxygen mobility which was facilitated by the coherent interface. Active sites at the interface were also considered to be in an excited, metastable state.

In work by other researchers, the high catalytic activity of a specific multiphase molybdate catalyst was attributed to the formation of a "pseudo-single-phase" material (a saturated solid solution) at the interfacial region. This interfacial material was believed to have the necessary active centers in close proximity (11–17). For solid solutions of $Bi_{2-x}Ce_x(MoO_4)_3$, the active centers were identified with particular metal ion sites (e.g., Bi^{3+}, Mo^{6+}, Ce^{3+}) which were responsible for hydrocarbon chemisorption, hydrogen abstraction, oxygen insertion, and reoxidation of the reduced oxide surface (11). The occurrence of specific structurally coherent interfaces was also stipulated, based on calculations of disregistery and lattice misfit of the lower Miller index planes. The authors indicated that an interfacial material should exist having a nonuniform composition which was different from the two phases which formed the interface. Thermodynamic calculations of the free energy

[1] To whom correspondence should be addressed.

0021-9517/96 $18.00

of mixing of the phases (relative to saturated solutions) were correlated with catalytic activity. The occurrence of the solid solution at the interface was believed to enhance lattice oxygen diffusion for a catalytic redox cycle (Mars–van Krevelen mechanism).

In other work on multiphase $Bi_2(MoO_4)_3$–MoO_3 catalysts, a specific crystallographic incorporation of bismuth molybdate on MoO_3 was believed to occur (18). Impregnation of $Bi(NO_3)_3$ solutions on MoO_3 crystallites produced preferential distribution of Bi on the (100) and (001) edge planes of MoO_3; formation of a surface layer of $Bi_2(MoO_4)_3$ was proposed. For selective oxidation of propene, Bi^{3+} sites at the surface were proposed to be responsible for hydrocarbon adsorption or activation; an allylic intermediate was believed to migrate to the (010) MoO_3 plane where addition of oxygen occurred (19–21). The yield of acrolein depended on the coverage of Bi on the MoO_3. Although characterization of this multicomponent molybdate system was rather limited, formation of other phases or variations in structure or composition were not believed to occur.

The importance of a remote control mechanism has been discussed in a large number of papers dealing with many multicomponent selective oxidation catalysts (1, 22–27). In this approach, the role of different phases has been interpreted in terms of donor and acceptor functions. The existence of a surface mobile oxygen species has been postulated which can spillover from the donor to the acceptor phase: the catalytic performance of the acceptor phase is affected by the resulting modification of the local structure or coordination of the surface atoms. For example in a study of the multicomponent α-Sb_2O_4–MoO_3 system involving labeling experiments (24), an enhancement in catalytic activity for propene oxidation was explained by classifying MoO_3 as the acceptor phase and α-Sb_2O_4 as the donor phase. The catalysts were prepared in such a way that no "mutual contamination" of the materials was believed to occur: specifically, techniques such as low temperature synthesis and mechanical grinding were believed to avoid the formation of a coherent interface or interfacial material. It was proposed that a maximum in catalytic activity was obtained when the surface areas of the donor and acceptor phases in the multiphase catalysts were comparable; some "contact" among particles of the different phases was believed to be essential in order to facilitate the transportation of the spillover oxygen species.

In our earlier research on multicomponent molybdate catalysts, we established that there were synergetic effects for $NiMoO_4$–MoO_3 materials used to oxidize 1-butene to maleic anhydride (28–30). $NiMoO_4$ with 15–40% "excess" MoO_3 exhibited higher selectivity and activity compared to the single component materials. Characterization of these precipitated or impregnated multicomponent catalysts revealed a spreading of $NiMoO_4$ on the surface of MoO_3 crystallites. Other multiphase molybdate materials have also been examined and similar results have been obtained (31, 32). For some of these systems, the role of each phase has been considered. For the $MnMoO_4$–MoO_3 system, it was suggested that MoO_3 was efficient in providing lattice oxygen but was less capable of reoxidation through chemisorption of gas phase oxygen; $MnMoO_4$, on the other hand, exhibited a high uptake of gas phase oxygen. Detailed structural and compositional information at the interfaces of precipitated or impregnated multicomponent molybdate materials has been difficult to obtain, due in part to the many types of morphologies and contacting patterns which occur.

We have recently developed a new catalyst preparation technique based on the reactive sputtering of thin film which can be used to address some of the questions regarding multicomponent metal oxide catalysts. The materials which are produced have a more well-defined "architecture" which restricts the types of morphologies and contacts (33). The sputtering technique also inherently produces films which are more closely contacted since growth occurs at the "atomic" level. Depositions can be directly made on specific substrate surfaces. There are also important advantages in performing characterization because the planar nature of these samples makes the application of some techniques more feasible.

2. EXPERIMENTAL

2.1. Preparation of Catalytic Films by Reactive Sputter Deposition

A planar magnetron sputtering system (Plasmatron Coating & Systems Inc.) was used to deposit films of MoO_3, $NiMoO_4$, or combinations of these materials (34). Three power sources were available for operating the target guns: an RF source operated at 13.56 MHz with a maximum power of 500 W and two DC sources (controlled separately) with maximal operation of 600 V and 1.5 A. The sputtering chamber was evacuated to below 10^{-7} Torr using a mechanical pump and a cryopump prior to presputtering of the target and film deposition. Flow rates of Ar (ultrahigh purity, Matheson) and O_2 (zero grade, Air Products) were regulated by mass flow controllers (MKS) between 6 and 50 sccm. The water-cooled sputtering guns used metal targets of Mo ($2'' \times 0.25''$, 99.99%, Superconductive, Inc.) and Ni ($2'' \times 0.0625''$, 99.99%, Superconductive, Inc.); the targets were mounted at 40° angles normal to the deposition plane, and the guns could be operated simultaneously or sequentially. The distance between the targets and the deposition plane was 8.5 cm^{-1}. During deposition, the pressure within the sputtering chamber could be controlled between 3 and 50 mTorr using a bypass throttle valve (MKS). The residual gas analyzer system (Quadrex 200, Leybold Inficon) was used to monitor the chamber environment prior to and during deposition.

TABLE 1

Deposition Parameters for Films

Sample	RF (W)/target	DC-1 (mA)/target	DC-2 (mA)/target	Ar flow (sccm)	O_2 flow (sccm)	T (°C)	P (mTorr)	Time (min)
A	100/Mo	—	—	8	24	415	5.0	30
B	—	150/Mo	170/Ni	6	25	525	8.0	30
C	100/Mo	—	—	8	24	415	8.0	30
	—	150/Mo	170/Ni	6	25	525	8.0	8
D	100/Mo	—	—	8	24	415	8.0	30
	—	150/Mo	170/Ni	6	25	525	8.0	20
E	—	150/Mo	170/Ni	6	25	525	8.0	30
	100/Mo	—	—	8	24	415	8.0	30
F[a]	—	150/Mo	170/Ni	6	25	525	8.0	30

[a] Followed by heating to 625°C.

Silicon wafers ($2'' \times 0.12''$, *n*-type, Recticon) were used as the inert carriers for the catalytic materials. No attempt was made to remove the surface layer of SiO_2 which typically forms after exposure of Si surfaces to ambient laboratory conditions. The wafers had no activity for 1,3-butadiene conversion and were selected because of advantages in sample characterization. (For one technique, laser Raman spectroscopy, weak bands were present in the 940–1000 cm^{-1} region of the spectrum due to SiO_2; however, this did not significantly impede characterization of the catalyst thin films). The wafers were placed on a graphite susceptor which could be rotated during deposition; an induction heating system was designed to allow samples to be heated up to 1100°C. The deposition temperature was measured by placing a thermocouple directly above the wafer and was controlled by varying the RF-power supplied to the induction heater. Calibration of the thermocouple was performed by correlating the melting points of different metals (150 to 700°C) with the thermocouple readings.

Deposition conditions for preparing single phase and multilayer films (samples A–F) are summarized in Table 1. The deposition processing parameters which could be varied directly included current or power delivered to the sputtering guns, flow rates of Ar and O_2, system pressure prior to and during sputtering, substrate temperature, and deposition time. As has been observed for the deposition of many metals, metal oxides, and metal sulfides, these parameters have a complex relationship to the composition, structure, and growth rate of the materials. The specific effects for the materials used in this study are discussed in more detail elsewhere (34). The parameters provided in Table 1 represent "optimal" conditions for single phase and multilayer films based on repetitive preparation and characterization studies.

These films consisted of α-MoO_3, α-$NiMoO_4$, and β-$NiMoO_4$ (and combinations thereof). Single-phase films were used as-prepared for characterization (next section) and comparison with published reference data. However, β-$NiMoO_4$ (sample F) films could not be prepared directly using reactive sputtering because of the high temperatures required for this metastable phase. β-$NiMoO_4$ also transforms to α-$NiMoO_4$ at temperatures below 300°C (35, 36), and therefore the use of some of the characterization techniques was not possible. A two-step strategy which involved both sample preparation and *in situ* characterization was used successfully. First, α-$NiMoO_4$ was deposited according to the conditions used for sample B; then, the films were transferred to a high temperature laser Raman cell (37), and the $\alpha \rightarrow \beta$ phase transformation was induced at 625°C. *In situ* laser Raman characterization was obtained after the samples were cooled to 450°C, corresponding to the reaction temperature used for the catalytic studies: no $\beta \rightarrow \alpha$ transformation was observed to occur.

2.2. Catalyst Characterization

2.2.1. X-ray diffraction (XRD). XRD measurements were performed using a Scintag 2000 diffractometer with Cu$K\alpha$ radiation. The diffraction patterns were recorded using θ–2θ scans between 10 and 50° with a 0.03 (2θ) step size and a 2.5-sec count time per step. The accuracy of obtained *d* spacing values was dependent on diffraction intensity of the thin films: for α-MoO_3 it was estimated to be close to 0.01, whereas for α-$NiMoO_4$ and β-$NiMoO_4$ the accuracy was about ± 0.04.

2.2.2. Laser Raman spectroscopy (LRS). Laser Raman spectra were obtained in a 90° reflection mode using a Spex 1877 Triplemate monochromator, a Spectra Physics 164 Ar ion laser (operating at 514.4 nm and 50–200 mW at the source), and a CSMA data acquisition system (Princeton Instruments, Inc.).

2.2.3. X-ray photoelectron spectroscopy (XPS). XPS was performed using a Physical Electronics Industries 5500 multitechnique surface analysis system (Perkin Elmer) operated with Al$K\alpha$ radiation. All spectra were referenced to a C 1s binding energy of 284.0 eV.

2.2.4. X-ray fluorescence spectroscopy (XRF). XRF data were obtained using a Siemens SRS 200 X-ray spectrometer. The analysis was performed by measuring the net $K\alpha$ X-ray intensities of Ni and Mo excited by a Cr radiation source. Pure-metal thin films of Ni and Mo deposited on Si with known thickness were used as standards to determine the empirical parameters for compositional analysis (38).

2.2.5. Scanning electron microscopy (SEM). SEM micrographs were obtained using a JEOL JSM-840A scanning electron microscope operating at 15 kV and 10- to 30-kx magnification. A 200-Å gold layer was sputtered on samples to increase the conductivity.

2.2.6. Transmission electron microscopy (TEM). TEM electron diffraction and morphology micrographs were obtained using a Phillips CM-30 transmission electron microscope operating at 300 kV which provided magnification up to 160 kx. The TEM specimens ere prepared by etching the back of the Si carrier. Selected area diffraction patterns (SAD) were obtained using SAD apertures of 5 and 10 μm. Convergent beam diffraction patterns (CBD) were performed and involved apertures between 20 to 100 nm.

2.3. Reactor Studies

Oxidation of 1,3-butadiene using the thin film catalysts was studied in a continuous flow reactor at 450°C. The wafers were reduced to a size of 1 to 3 mm using a diamond cutter; about 5 to 15 g of material was loaded into a passivated 1/2″ od stainless steel tube reactor to form a small fixed bed. The amount of material used was adjusted to give approximately equal conversions of 1,3-butadiene (about 11–13%) for each study. The total gas flow rate to the reactor (regulated by Model FC-260 Tylan mass flow controllers) was 50 cm^3/min and was composed of 3% 1,3-butadiene (Matheson, industrial grade), 20% oxygen (Air Products, zero grade), and the remainder He (Air Products, zero grade). An on-line quadrupole mass spectrometer (UTI, 100C) was used to analyze the gases; a glass, single-stage molecular jet separator (SGE) was used (39). The catalyst was heated to 450°C for 1 h in flowing He prior to introducing the 1,3-butadiene and oxygen flows. Steady-state results were achieved after about 30 min of reaction; catalytic activity and selectivity were observed to be constant over 5 h.

3. RESULTS

3.1. Characterization and Catalytic Activity of α-MoO_3 Thin Films

Thin films of α-MoO_3 (sample A) were produced at substrate temperatures between 375 and 425°C, deposition pressures between 5 and 10 mTorr, and O_2 and Ar flow rates of 8 and 24 sccm, respectively. At substrate temperatures higher than 450°C, no deposition of any material was detectable. The deposition pressure affected both morphology and crystal size: at 5 mTorr, relatively smooth, basal-oriented films were produced (which were used in most studies). The O_2/Ar flow rate ratio was 3 or greater in order to avoid the formation of other "molybdenum-oxide" materials (not necessarily identifiable phases); crystallinity was also better at these ratios.

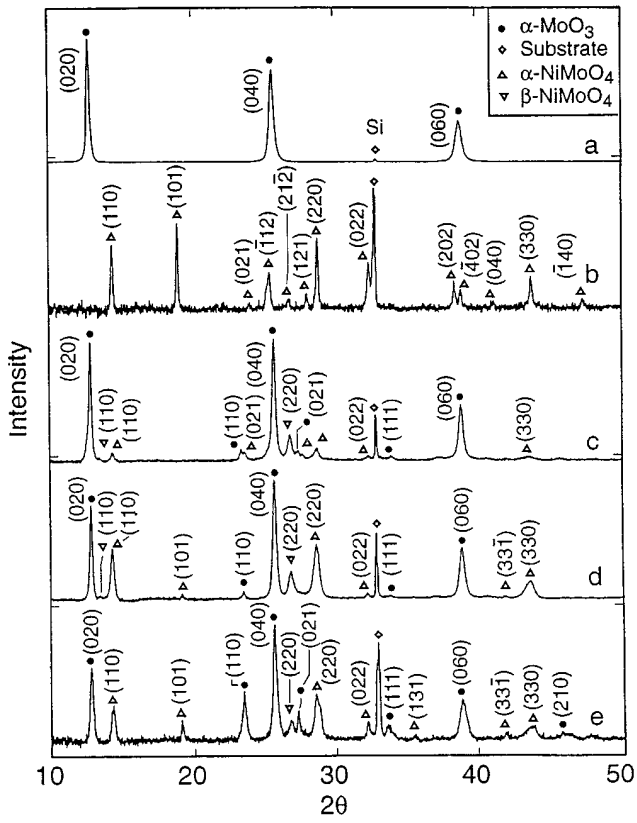

FIG. 1. XRD of thin films deposited on Si: (a) α-MoO_3, (b) α-$NiMoO_4$, (c) $NiMoO_4$ (8 min deposition) on α-MoO_3, (d) $NiMoO_4$ (20 min deposition) on α-MoO_3, and (e) α-MoO_3 on $NiMoO_4$.

XRD characterization of films deposited at 415°C (Fig. 1a, Table 2) revealed that α-MoO_3 was formed. The d spacings at 6.93, 3.46, and 2.31 closely matched those for (020), (040), and (060) reflections, respectively, based on the α-MoO_3 powder diffraction pattern standard (40). The intensity of these peaks and the absence of other bands revealed that the sample was strongly oriented. The peak at $2\theta = 32.9°$ was due to the Si carrier.

Formation of α-MoO_3 was also identified by LRS due to peaks at 667, 820, and 995 cm^{-1} in the laser Raman spectrum (Fig. 2a, Table 3). The low wavenumber portion of the spectrum was somewhat reduced in intensity, but peaks at 116, 131, and 159 cm^{-1} could be observed which also corresponded to α-MoO_3. The peaks at 300 and 520 cm^{-1} and the broad band extending from approximately 940 to 1000 cm^{-1} were attributed to the carrier.

TABLE 2

***d* Spacings of Films**

Sample	*d* (Å)	Sample	*d* (Å)	References	*d* (Å)	References	*d* (Å)
A	6.93	D	6.93	α-MoO_3	6.921	β-$NiMoO_4$	3.791
	3.46		6.68		3.808		3.466
	3.71		6.20		3.464		3.342
	2.31		4.66		3.440		3.262
B	6.20		3.81		3.259		3.125
	4.66		3.47		3.008		2.776
	3.72		3.34		2.703		2.651
	3.52		3.10		2.653		2.431
	3.27		2.75		2.608		2.306
	3.19		2.71		2.309		2.231
	3.11		2.66		2.271		2.067
	2.74		2.31		1.995		1.923
	2.71		2.16		1.958	NiO	2.412
	2.34		2.07		1.905		2.089
	2.31	E	6.93		1.732		1.477
	2.09		6.19	α-$NiMoO_4$	6.19		1.476
	2.06		4.66		5.50		1.259
	1.94		3.81		4.665		1.206
C	6.93		3.46		4.373		1.205
	6.65		3.34		4.085		1.044
	6.21		3.26		3.721		
	3.81		3.09		3.711		
	3.74		2.75		3.513		
	3.47		2.71		3.193		
	3.33		2.66		3.095		
	3.26		2.46		2.769		
	3.19		2.31		2.746		
	3.10		2.15		2.727		
	2.75		2.07		2.465		
	2.71		1.96		2.331		
	2.66				2.323		
	2.31				2.188		
	2.07				2.154		
					2.062		
					1.916		

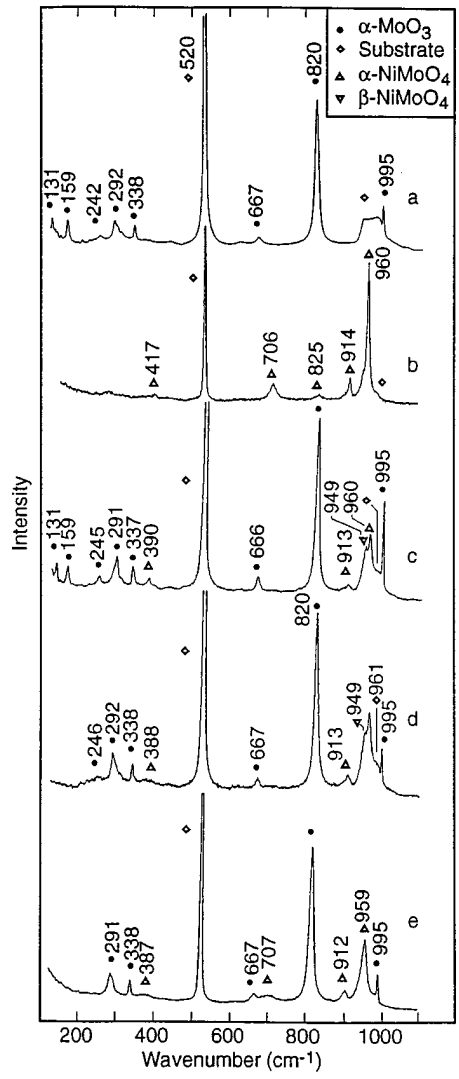

FIG. 2. Laser Raman spectra of thin films deposited on Si: (a) α-MoO_3, (b) α-$NiMoO_4$, (c) $NiMoO_4$ (8 min deposition) on α-MoO_3, (d) $NiMoO_4$ (20 min deposition) on α-MoO_3, and (e) α-MoO_3 on $NiMoO_4$.

XPS binding energies (Table 4) for Mo $3d_{3/2}$ at 232.7 eV, Mo $3d_{3/2}$ at 235.5 eV, and O 1s at 530.4 eV were also in close agreement with other reports for α-MoO_3 (41).

SEM of the α-MoO_3 films (Fig. 3a) revealed a fairly smooth morphology with grain sizes of about 0.2–0.5 μm. Edge views (Fig. 4a) indicated that the layer-like microstructure was relatively dense.

Conversion of 1,3-butadiene over the α-MoO_3 films was high (Table 5), but the selectivities for partial oxidation products such as furan, 2(5*H*)-furanone, and maleic anhydride were low. Postreaction characterization by LRS and XPS revealed that the films were unchanged.

For a few studies, α-MoO_3 films with (110) and (010) orientations were prepared for use with samples also involving $NiMoO_4$ (Section 3.3). To produce these films, the substrate temperature was 375°C, the deposition pressure was 5 mTorr, and the Ar and O_2 flow rates were 8 and 24 sccm, respectively. XRD characterization data for the multiphase films is summarized below; further discussion of the characterization data is provided elsewhere (34).

3.2. Characterization and Catalytic Activity of α-NiMoO4

Thin films of α-$NiMoO_4$ (sample B) were deposited by simultaneous DC-sputtering of Ni and Mo targets. To produce α-$NiMoO_4$, the substrate temperature was maintained at 525°C, the pressure was 8 mTorr, and the flow rates of Ar and O_2 were 25 and 6 sccm, respectively. This deposition temperature was much lower than typical solid-state synthesis which require heating mixtures of NiO and α-MoO_3 and Mo(metal) at 800°C for up to 8 h (42). The effects of other sputtering parameters on deposition rate and grain size were similar to those observed for α-MoO_3 deposition.

TABLE 3

Raman Bands (cm^{-1}) of Thin Films Deposited on Si/SiO_2 Substrate

	Raman bands observed (cm^{-1})
Sample	
A	116, 131, 159, 242, 292, 300(br),[a] 338, 471(w), 520(vs),[a] 667, 820, 995, 1000–940(br)[a]
B	417(w), 520(vs),[a] 706, 825, 914, 960, 1000–980(sh)[a]
C	131, 159, 245, 291, 337, 390(w), 520(vs),[a] 666 (w), 819, 896(sh), 913, 949, 960, 980(sh),[a] 995
D	246, 292, 338, 388(w), 520(vs),[a] 667, 820, 897(sh, w), 913, 949, 960, 980(sh),[a] 995
E	291, 338, 387, 520(vs),[a] 667, 707, 820, 912, 959, 995
F	196(w), 294, 307, 351, 378, 392, 521, 830, 872, 895, 904, 949, 959
Reference	
α-MoO_3 (28)	116, 131, 162, 198, 219, 247, 293, 338, 378, 474(w), 667, 820, 995
α-$NiMoO_4$ (28)	253, 266, 332, 371, 387, 419, 443, 494, 707, 825(vw), 914, 961
β-$NiMoO_4$	346, 376, 824, 886, 898, 944, 954

[a] Substrate peak.

XRD characterization (Fig. 1b, Table 2) indicated that the films were multicrystalline and randomly oriented and consisted of α-$NiMoO_4$. The strong diffraction intensities ($d = 6.20$, 4.66, and 3.52) corresponded closely to the (110), (101), and (112) planes of α-$NiMoO_4$. Multiple reflections of (220), (330), and (202) were also observed. Some peaks with lower diffraction intensity ($d = 3.72$, 3.27, 3.19, 2.74, 2.34, 2.31, 2.09, and 1.94) were also assigned to α-$NiMoO_4$ (42). It should be noted that diffraction from specific planes not reported for the powder diffraction pattern standard may be observed for thin films; however, the position of these diffraction peaks can be predicted from calculations based on the solid-state structure. Other low intensity diffraction peaks ($d = 2.74$ and 2.09) could be attributable to α-$NiMoO_4$, but these peaks are also similar to peaks for β-$NiMoO_4$.

Other characterization results were consistent with the presence of α-$NiMoO_4$. Laser Raman bands (Fig. 2b, Table 3) at 706, 825 (weak), 914, and 960 cm^{-1} clearly indicated the presence of α-$NiMoO_4$ (28, 35, 43). The bandwidth (FWHM) of the 960 cm^{-1} peak was 12 cm^{-1}, which was comparable to that for the precipitated catalysts (28). Raman bands expected for α-$NiMoO_4$ below 700 cm^{-1} were weak. The carrier had a strong Raman peak at 520 cm^{-1} and two broad bands near 300 cm^{-1} and the region of 940–1000 cm^{-1} (appearing as a "shoulder" in this spectrum). No other phases were detected, including α-MoO_3 which is a strong Raman scatterer.

TABLE 4

X-ray Photoelectron Spectroscopy Bonding Energies

	Mo $3d_{5/2}$	Mo $3d_{3/2}$	O 1s	Ni $2p_{3/2}$	Ni $2p_{1/3}$
Sample					
A	232.7	235.5	530.4	—	—
B	232.9	235.5	530.6	856.4	874.1
C	232.4	235.6	530.8	855.9	873.8
D	232.4	235.9	530.7	856.1	874.0
E	232.9	234.9	530.7	—	—
Reference					
MoO_3 (41)	232.7	235.8	530.9		
α-$NiMoO_4$ (43)	232.5	235.6	530.7	856.3	873.8
NiO (44)			530.8	854.0/855.8	872.6

XPS binding energy data (Table 4) agreed with previously reported information for α-$NiMoO_4$ (43). Comparison of XPS characterization for NiO (specifically Ni $2p_{3/2}$ bands at 854.0 and 855.8 eV) indicated that this phase was not present (44).

SEM microscopy (Fig. 3b) showed that the polycrystalline film had a fairly uniform grain size of 0.1 μm. The film appeared to grow with a columnar morphology.

The α-$NiMoO_4$ films had a relatively high furan selectivity (16.5%), approximately twice that of α-MoO_3 (Table 5). However, the 1,3-butadiene conversion rate was relatively low. Compared to precipitated catalysts, the activity of the thin films was higher, based on the rate per unit surface area.

Films deposited at different relative DC currents were investigated because of the possible formation of NiO–$NiMoO_4$ solid solutions (other sputtering parameters were maintained the same as for sample B). NiO is also known to stabilize β-$NiMoO_4$ at temperatures as low as room temperature. XRF was used to determine the Ni/Mo elemental ratio for these films (Table 6). For thin films with Ni/Mo < 1, Raman bands associated with α-$NiMoO_4$ were apparent at 909 (914) cm^{-1} and 960 (961) cm^{-1}; the Raman spectra (Figs. 5a and 5b) also exhibited broad, weak bands, for example at 810–850 cm^{-1}, which may be an indication of a molybdenum-oxide material coexisting in the predominantly α-$NiMoO_4$ films. The relative intensity of these bands decreased as the Ni/Mo ratio approached the stoichiometry for α-$NiMoO_4$. For thin films with Ni/Mo > 1, the Raman spectra (Figs. 5d and 5e) exhibited peaks at 949 and

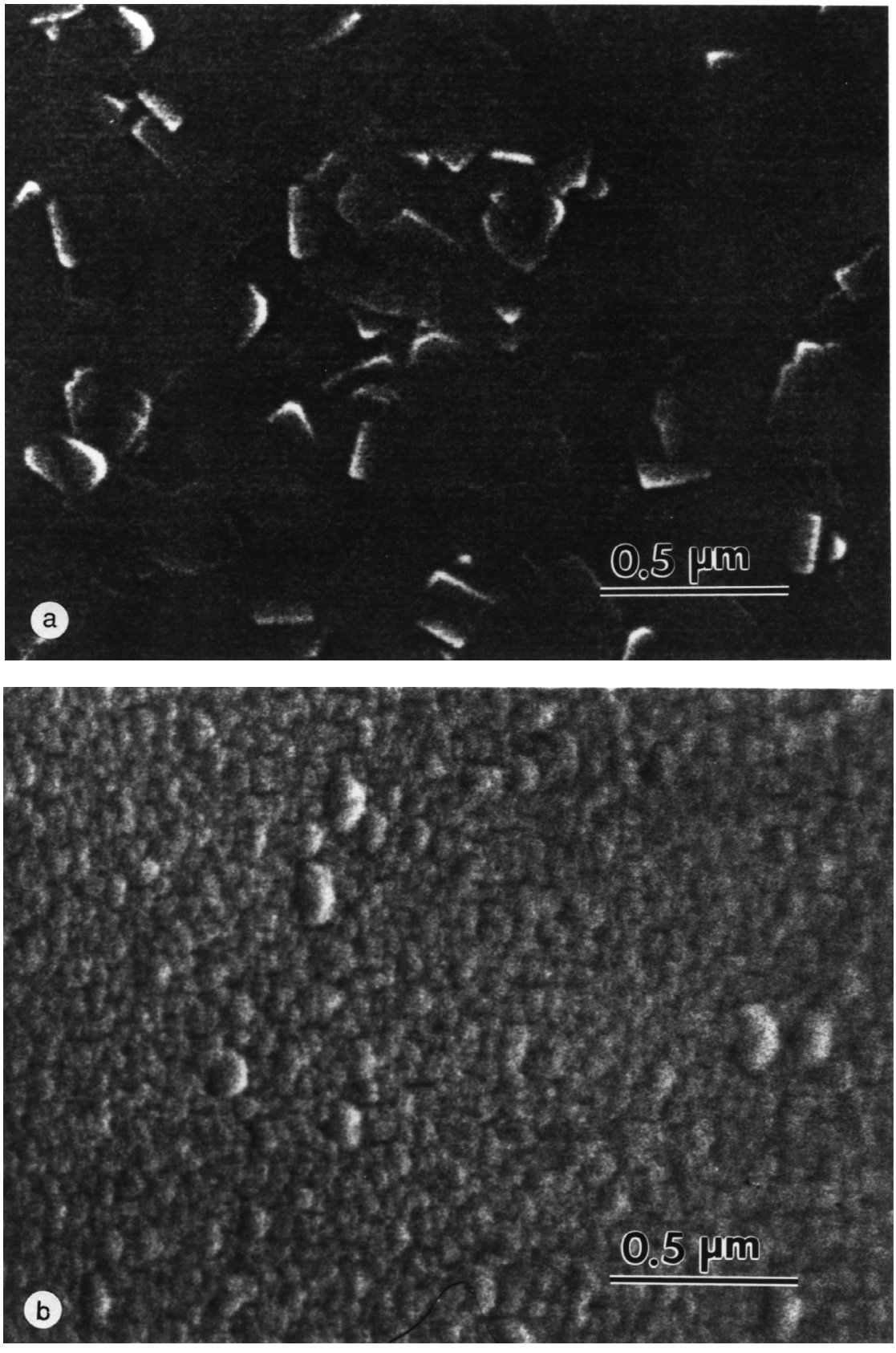

FIG. 3. SEM surface view of thin films on Si: (a) α-MoO_3, (b) $NiMoO_4$.

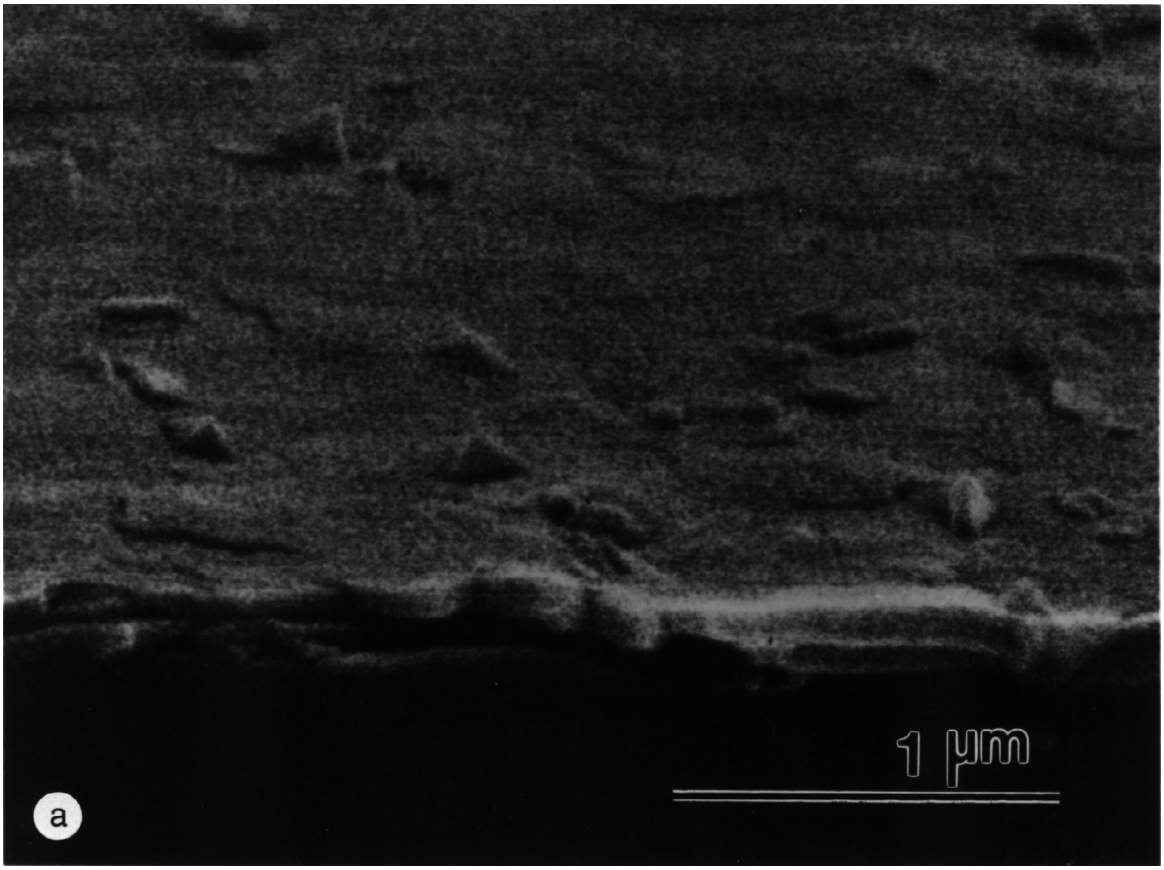

FIG. 4. SEM edge view of thin films on Si: (a) α-MoO_3, (b) $NiMoO_4$ on α-MoO_3, and (c) α-MoO_3 on $NiMoO_4$.

960 cm^{-1}. It was also observed that there was a change in the relative intensities of the 949 cm^{-1} peak (increase) and of the 706 cm^{-1} peak (decrease) with an increase in Ni/Mo ratio. This is indicative of the formation of β-$NiMoO_4$: characterization of β-$NiMoO_4$ in this study (Section 3.5) and other reports (43) has demonstrated that Raman bands are present at 960 and 949 cm^{-1} (having approximately equal intensity). In comparison with α-$NiMoO_4$, no peak was observed at 706 cm^{-1}, and the peak near 830 cm^{-1} was stronger than the 825 cm^{-1} band of α-$NiMoO_4$. The "excess" Ni in these films may have existed as a crystalline or amorphous nickel oxide material. This was a concern because formation of a NiO–$NiMoO_4$ solid solution has been reported to promote the formation of β-$NiMoO_4$. XRD did not provide effective characterization of the "excess" Ni since the (110) d spacing of β-$NiMoO_4$ varies in only a rather small range (between 3.33 and 3.34 Å) depending on the excess amount of NiO (36). In addition, NiO films typically were only weak diffracting, and significant peak overlap occurred with the $NiMoO_4$ phases. NiO is also a poor Raman scatterer. In contrast to the limited use of XRD and LRS, the ability to detect NiO with XPS was rather high based on the observation of the "split" Ni $2p_{3/2}$ peaks (44). XPS results for Ni/Mo > 1 films did not indicate the presence of NiO, suggesting that the oxidation state of "excess Ni" did not correspond to NiO.

3.3. Characterization and Catalytic Activity of $NiMoO_4$ on α-MoO_3 films

$NiMoO_4$ was deposited on α-MoO_3 using sputtering parameters related to the single phase processing conditions. For samples C and D in Table 1, (010) α-MoO_3 was deposited first using the conditions for producing sample A. $NiMoO_4$ was then deposited based on the sputtering parameters for sample B: two different sputtering times were used (8 and 20 min for samples C and D, respectively).

XRD results for samples C and D are given in Fig. 1c and 1d and in Table 2. Formation of α-MoO_3 was identified in both samples ($d = 6.93$, 3.44, 2.31). In addition to these strong (0k0) diffraction peaks, diffraction corresponding to (110) and (111) planes was also observed ($d = 3.81$ and 2.66) at lower intensity. Characteristic peaks for β-$NiMoO_4$ ($d = 6.65$ and 3.34) were observed for these multicomponent films (45, 46). For longer deposition times (sample D), the relative intensity of the main β-$NiMoO_4$ peak ($d = 3.34$) appeared to decrease. XRD peaks corresponding to α-$NiMoO_4$ could be identified ($d = 3.74$, 3.19, and 2.75 for sample C and $d = 4.66$, 2.75, and 2.16 for sample D),

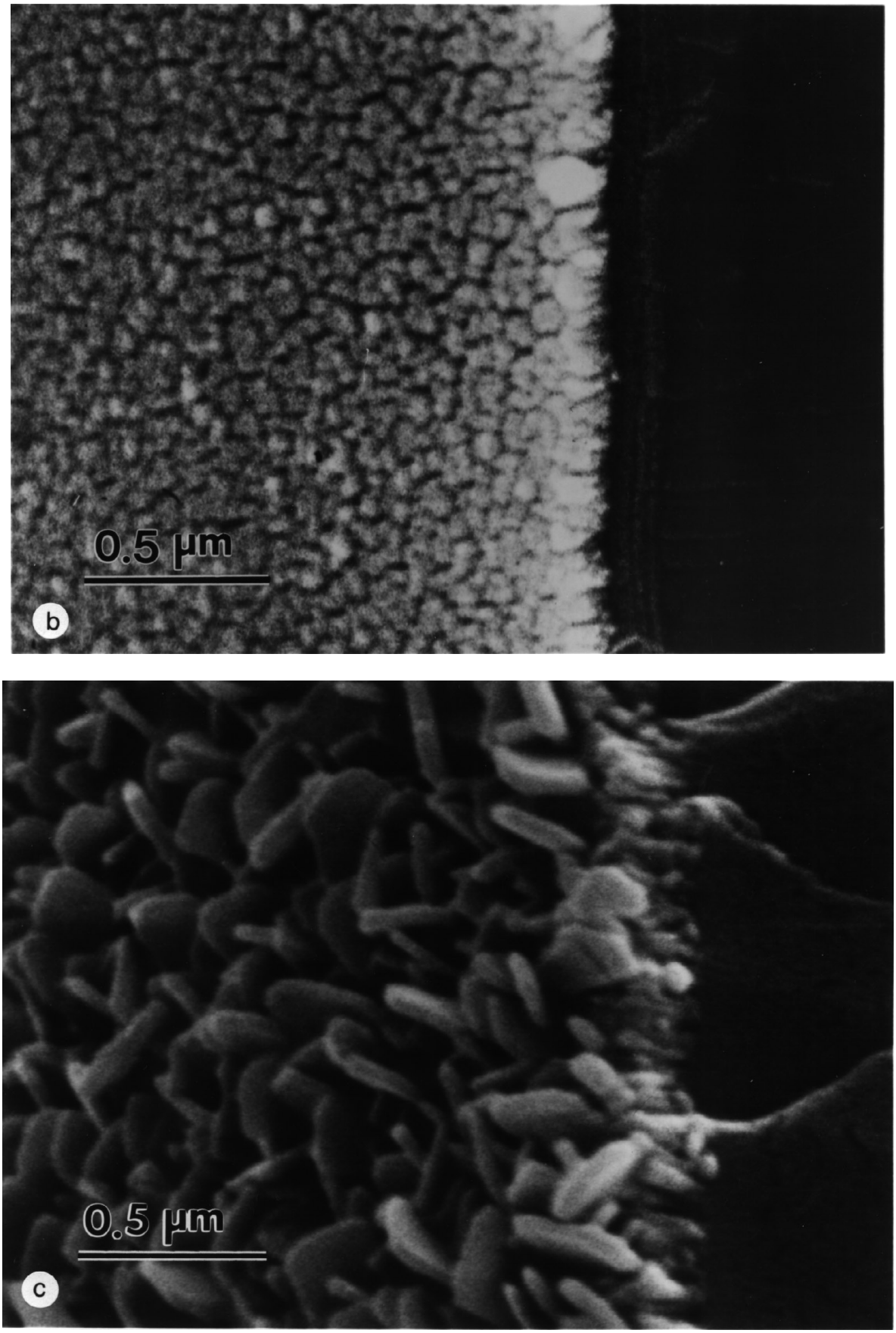

FIG. 4—*Continued*

TABLE 5

Conversion Rates and Selectivities for 1,3-Butadiene Oxidation: Sputtered Samples (A–F) and Selected Precipitated Catalysts (29)

	Sample						$NiMoO_4$ (prec.)	$NiMoO_4$ + 15% MoO_3 (prec.)
	A	B	C	D	E	F		
Rate ($g \cdot mol \cdot /min\text{-}m^2$) of 1,3-butadiene disappearance	1.86×10^{-3}	8.37×10^{-4}	1.16×10^{-3}	2.04×10^{-3}	2.65×10^{-3}	1.10×10^{-3}	6.9×10^{-3}	1.08×10^{-5}
Conversion (%) of 1,3-butadiene	12.4	11.2	11.5	12.2	13.1	13.2	66.2	79.2
Selectivity (%)[a]								
Furan	8.1	16.0	24.8	27.5	17.4	17.7	2.7	3.09
2(5*H*)-furanone	5.9	6.7	8.6	8.5	6.9	8.3	—[b]	—[b]
Maleic anhydride	6.2	9.3	13.5	14.7	12.1	10.7	0	32.5
CO/CO_2	68.4	51.9	44.0	42.6	58.4	51.1	37.3	16.8

[a] % Selectivity = (moles of product/moles of 1,3-butadiene consumed) $\cdot \frac{1}{\gamma} \cdot 100\%$, where γ is the ratio of C atoms in the reactant to the number of C atoms in the product.

[b] Not detected.

especially at the longer deposition time; multiple reflections for (110), (220), and (330) planes were present. Some low intensity peaks could be attributable to either α- or β-$NiMoO_4$ ($d = 2.75$ and 2.07), although the $d = 2.07$ peak should probably be considered to be an α-$NiMoO_4$ multireflection of (110). For these films, no formation of NiO was observed.

The Raman spectra for these samples (Figs 2c and 2d, Table 3) revealed peaks for β-$NiMoO_4$ at 949 and 960 cm^{-1} (see Section 3.5). Some bands which should be moderately intense could not be clearly discerned, such as at 830 (probably obscured by the MoO_3 band at 820 cm^{-1}), 895, and 904 cm^{-1} (43, 47). The 960 cm^{-1} band is indicative of the presence of α-$NiMoO_4$, but other bands characteristic of this phase were not present or were relatively weak (706 and 914 cm^{-1} for example), especially for the shorter deposition time (sample C). The Raman spectrum for sample D with 20 min deposition of $NiMoO_4$ on MoO_3 provided a much clearer indication of the presence of α-$NiMoO_4$, due to the greater intensity of the 914 cm^{-1} band. The 960 cm^{-1} peak was broadened for these films compared to single phase films.

TABLE 6

Ni/Mo Determined by XRF

DC currents (mA)		Atomic ratio of
Ni	Mo	Ni/Mo
85	150	0.767
100	150	0.864
150	150	0.932
170	150	0.984[a]
200	150	1.37
250	150	1.44

[a] Sample B. All other deposition parameters (i.e., other than DC currents) were the same as sample B, as given in Table 1.

An important observation about these results was that diffraction from other orientations of α-MoO_3, such as (110), (021), and (111), was observed. Restructuring of the α-MoO_3 edge planes at the interface may have occurred during the deposition of the $NiMoO_4$ material. It is also possible that some additional MoO_3 was formed during the simultaneous sputtering of Ni and Mo: growth involving different orientations of MoO_3 may have occurred. This would likely entail the formation of other nickel material (perhaps (NiO). Raman did not provide evidence for the presence of NiO: this may be due to very poor Raman scattering by NiO. Similarly, XRD did not reveal the presence of this phase, which would be difficult in any case due to the overlap between major peaks for NiO ($d = 2.089$ and $d = 2.412$) and $NiMoO_4$ ($d = 2.062$ and $d = 2.40$ based on structural calculations).

XPS binding energy data for these films (Table 4) was consistent with the formation of α-$NiMoO_4$ (as the overlayer material). The XPS results also did not indicate any NiO on the surface of the multicomponent films: no Ni $2p_{3/2}$ bands were present at 854.0 and 855.8 eV. The sensitivity of this technique probably indicated that NiO was not formed. Depth profiling by XPS indicated that the Ni/Mo ratio in the $NiMoO_4$ overlayer was constant, suggesting that the deposited $NiMoO_4$ was uniform.

SEM of these films (Fig. 4b) revealed that the $NiMoO_4$ material had a columnar growth structure. According to TEM (Figs. 6a and 6c) for sample C, the materials had a fairly smooth morphology with a fine grain structure. The SAD pattern (Fig. 6b) had d spacings appropriate for α-MoO_3, α-$NiMoO_4$, and β-$NiMoO_4$: the d spacings of 3.46 and 3.25 were attributable to α-MoO_3, d spacings of 6.20, 3.92, 3.52, 3.08, and 2.11 were attributable to α-$NiMoO_4$, and d spacings of 4.18, 3.35, 3.25, and 2.11 were attributable to β-$NiMoO_4$. It was recognized that the accuracy of d spacing for SAD was lower than that for XRD and that some specific SAD peaks may be absent in XRD

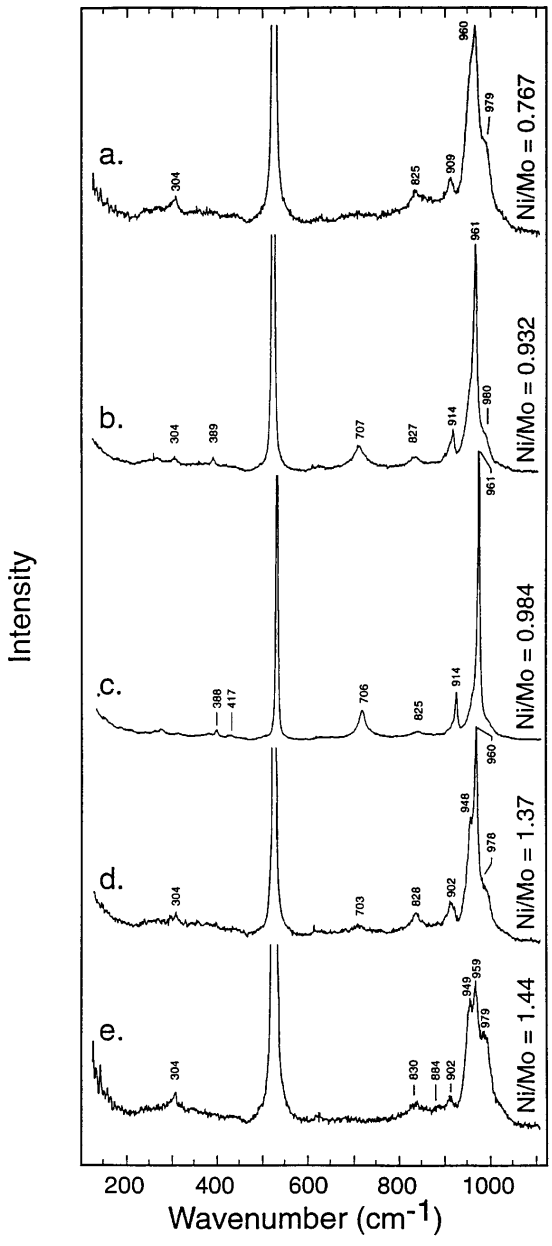

FIG. 5. Laser Raman spectra of Ni–Mo oxide films with different Ni/Mo stoichiometry by varying the sputtering current on Ni and Mo targets: (a) Ni/Mo = 0.767, (b) Ni/Mo = 0.932, (c) Ni/Mo = 0.984, (d) Ni/Mo = 1.37, (e) Ni/Mo = 1.44.

powder pattern. For some d spacings from SAD, overlap also made assignment difficult: $d = 3.25$ could be due to α-MoO_3 or β-$NiMoO_4$, and $d = 2.11$ could be assigned to α-$NiMoO_4$ or β-$NiMoO_4$. The existence of distinct phases could not be established by convergent beam diffraction even with an electron beam of 20 nm. For samples with more $NiMoO_4$ deposited (sample D), TEM characterization revealed that platelet crystals were formed having sizes between 0.1 and 0.5 μm; only a portion of the surface appeared to be covered. These structures were identified to be α-$NiMoO_4$ by using convergent beam electron diffraction of single grains (Figs. 7c and 7d). In contrast, the electron diffraction pattern of the areas in which these platelet structures were absent indicated that the previously described uniform, fine-grained material was present (Figs. 7e and 7f).

For these thin films of $NiMoO_4$ on α-MoO_3 (sample C and D), the selectivity for partial oxidation products (furan, 2(5*H*)-furanone, and maleic anhydride) increased significantly (Table 5). A higher 1,3-butadiene conversion rate was also observed for the multicomponent films as compared to α-$NiMoO_4$. Comparison of samples with 8- and 20-min depositions of the $NiMoO_4$ on α-MoO_3 revealed the selectivities to be similar: however, the 1,3-butadiene conversion rate was higher for the 20-min deposition (sample D). Compared to precipitated catalysts, the conversion rate for 1,3-butadiene and the selectivity for furan was much higher. Although the precipitated materials had a somewhat higher selectivity for maleic anhydride, no 2(5*H*)-furanone was produced.

Figure 8 provides the XRD patterns for $NiMoO_4$ deposited on the surface of α-MoO_3 with (110) and (010) orientations (8a) and with a preferred (010) orientation (8b). XRD peaks corresponding to both α- and β-$NiMoO_4$ were detected for both samples. However, the relative intensity of the characteristic β-$NiMoO_4$ peak ($d = 3.34$ Å) was lower for the deposition on (110)–(010) α-MoO_3; formation of α-$NiMoO_4$ was preferred.

3.4. Characterization and Catalytic Activity of α-MoO_3 on α-$NiMoO_4$

Thin films of α-MoO_3 on α-$NiMoO_4$ were also deposited by a sequential deposition process (sample E). α-$NiMoO_4$ was deposited first on the Si carrier based on the sputtering parameters for sample B; then α-MoO_3 was produced according to the deposition conditions for sample A.

The XRD pattern (Fig. 1e, Table 2) confirmed the presence of α-$NiMoO_4$, β-$NiMoO_4$, and α-MoO_3. The intense peaks of α-MoO_3 corresponded to the (0k0), (110), (021), and (111) planes. Therefore, the α-MoO_3 deposited on $NiMoO_4$ had a more multicrystalline orientation compared to the strong (010) α-MoO_3 orientation resulting for sample A; the relative intensity of the (110) peak was particularly high. XRD peaks corresponding to α-$NiMoO_4$ were observed ($d = 6.19$, 4.66, 3.09, 2.75, 2.26, 2.15, and 2.07), but β-$NiMoO_4$ was also identified by $d = 3.34$. A possible overlapping peak for α-$NiMoO_4$ or β-$NiMoO_4$ was present near $d = 2.75$. XRD indicated that the predominant nickel molybdate phase was α-$NiMoO_4$, but some transformation had occurred, probably at the interfacial region.

LRS (Fig. 2e, Table 3) confirmed the existence of α-MoO_3, but the bandwidth (FWHM) of the 960 cm^{-1}

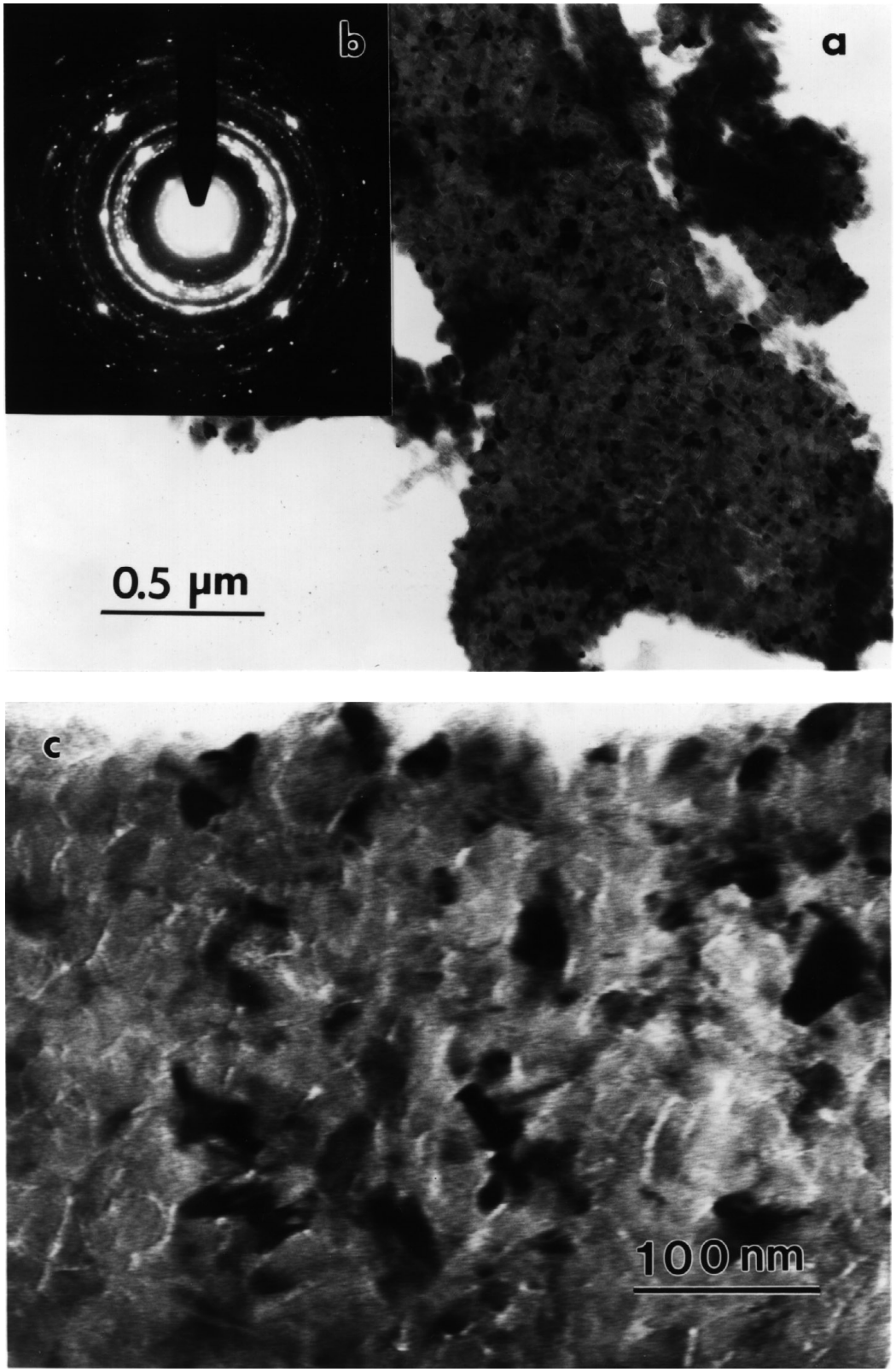

FIG. 6. TEM surface view of sample C, $NiMoO_4$ (8 min) on α-MoO_3 (30 min): (a) morphology at 50 kx, (b) SAD pattern of area (a), and (c) morphology at 200 kx.

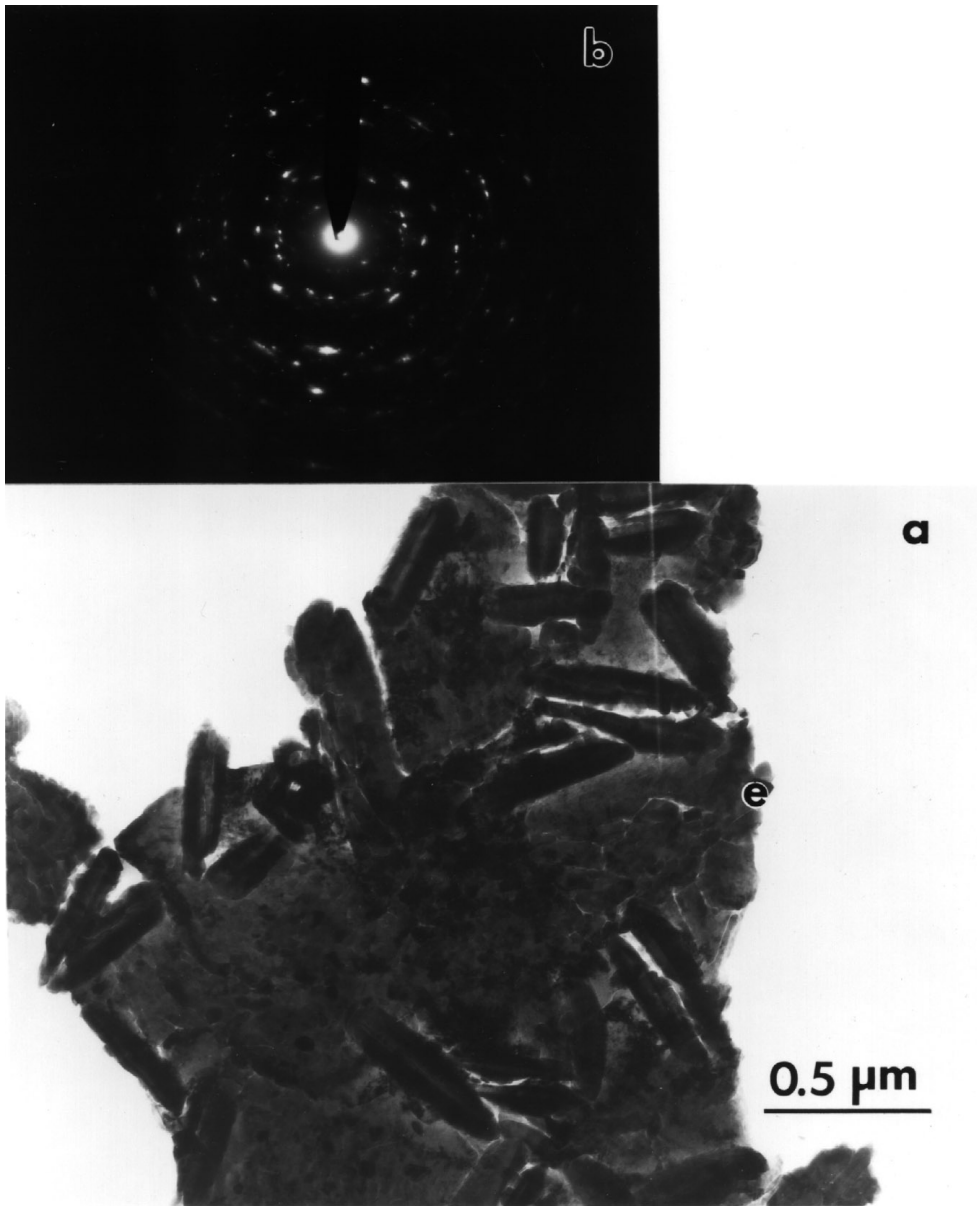

FIG. 7. TEM surface view of sample D. $NiMoO_4$ (20 min) on α-MoO_3 (30 min): (a) morphology at 25 kx, (b) SAD of area (a), (c) morphology of platelet crystal, α-$NiMoO_4$, (d) electron diffraction of platelet, α-$NiMoO_4$, (e) morphology of fine mixture area, and (f) electron diffraction of area (e).

peak of α-$NiMoO_4$ was very large (23 cm^{-1}); again, a structural transformation was indicated which may be considered to be the presence of a β-$NiMoO_4$-like material (although the 949 cm^{-1} band for this phase could not be clearly observed). This material was similar to that observed for samples C and D, although the relative amount was lower, perhaps due to the lower deposition temperature.

SEM (edge view in Fig. 4c) results clearly revealed that the α-MoO_3 deposited on the α-$NiMoO_4$ had several orientations. The crystal size of the α-MoO_3 layer appeared to be larger than that of the $NiMoO_4$.

For α-MoO_3 deposited on α-$NiMoO_4$, the highest conversion rate of 1,3-butadiene was observed. However, CO and CO_2 were produced in relatively large amounts, and the selectivities for furan, 2(5*H*)-furanone, and maleic anhydride were relatively low.

3.5. Characterization and Catalytic Activity of β-$NiMoO_4$ Films

Because the characterization of some films revealed the presence of β-$NiMoO_4$-like material, an attempt was made to produce thin films of this phase directly by reactive sputtering. A successful two-step process was employed

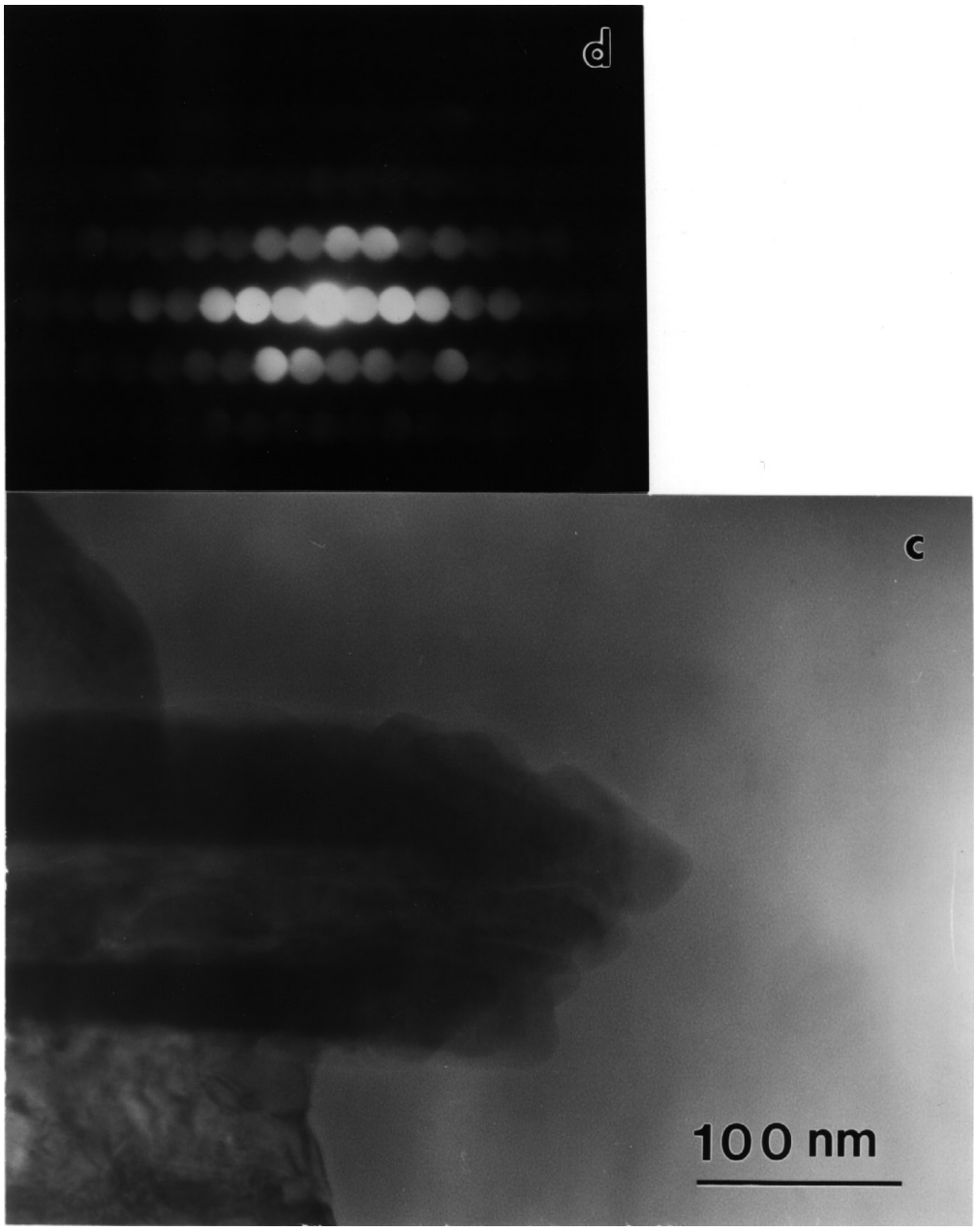

FIG. 7—*Continued*

to obtain the metastable, high temperature phase. First α-$NiMoO_4$ was deposited according to the sputtering parameters given for Sample B in Table 1; second, this material was then heated to 625°C to induce the $\alpha \rightarrow \beta$ transformation. The resulting material (sample F) was cooled to 450°C for laser Raman characterization and reactor studies.

The laser Raman characterization was performed *in situ* in a high temperature cell (37). The strongest Raman bands (Fig. 9) were at 949 and 959 cm^{-1}; peaks were also present at 830, 872, 895, and 904 cm^{-1}. Most of these bands (except perhaps for 830 and 959 cm^{-1}) were unique to the β-phase. A Raman band at 706 cm^{-1} which would correspond to α-$NiMoO_4$ was not present, and the intensity of the 830 cm^{-1} band (for β-$NiMoO_4$) was stronger than would be expected for the 825 cm^{-1} band (for α-$NiMoO_4$). Upon cooling to room temperature, transformation of the metastable (high temperature) β-phase to the stable (room temperature) α-phase was observed.

β-$NiMoO_4$ had similar selectivity compared to α-$NiMoO_4$, although the conversion rate for 1,3-butadiene was 30% higher.

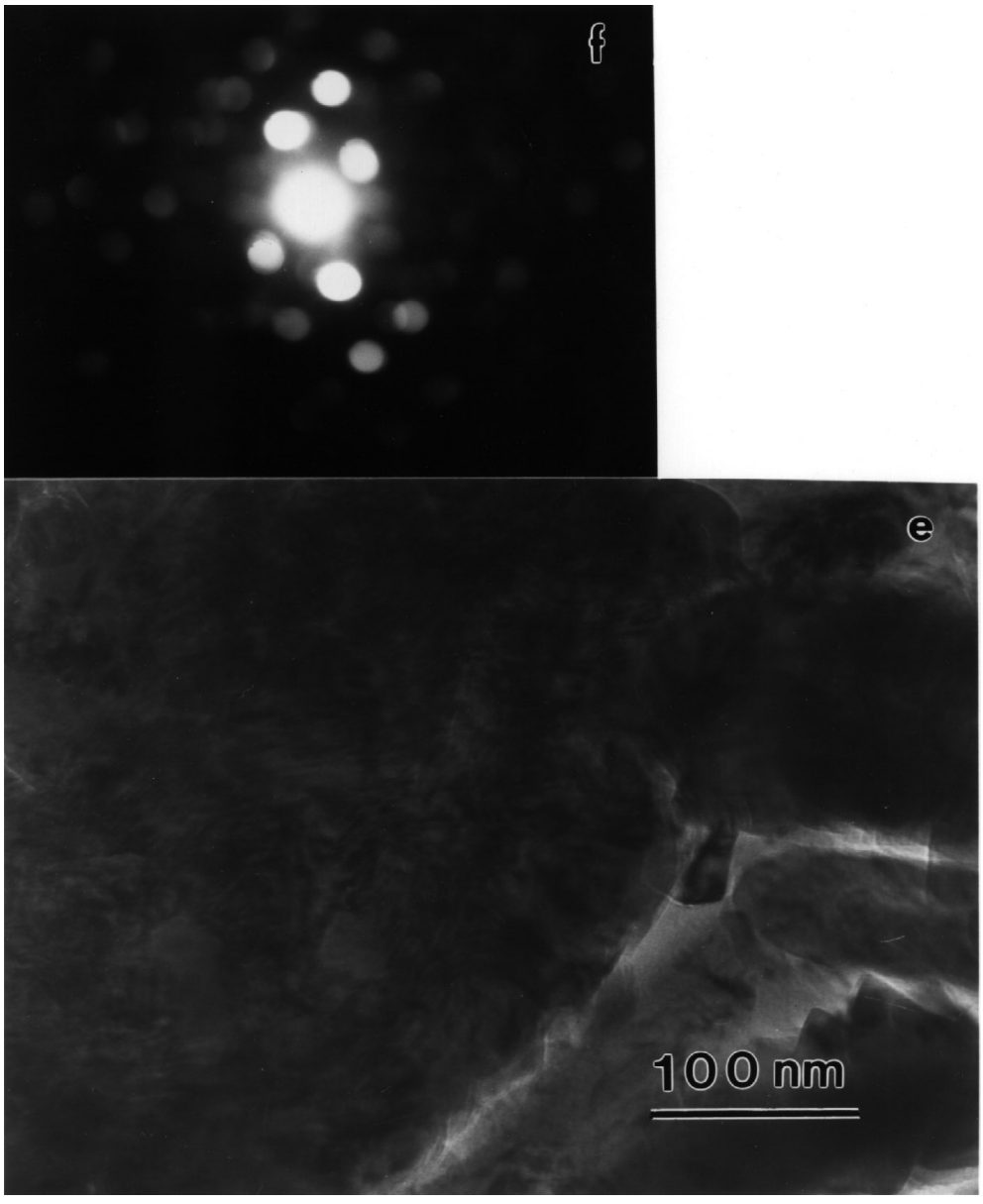

FIG. 7—*Continued*

4. DISCUSSION

In this research, reactive sputtering was used to produce multicomponent thin films having a close contact between phases which are known to be important components of catalysts for the selective oxidation of C_4 hydrocarbons to maleic anhydride (28–30). Single phase α-MoO_3 films produced by sputtering had a (010) orientation with a relatively smooth morphology. This preferred orientation would be expected on the Si carrier since growth should occur according to the strongest bonding in α-MoO_3. Because of this preference, most studies tended to emphasize growth on this surface. Single-phase α-$NiMoO_4$ films produced were polycrystalline and had a rather uniform crystal size of 0.1 μm. Based on thermodynamic information, α-$NiMoO_4$ should be formed for the multiphase films since this is the stable phase at the deposition temperature (less than 600°C). Cleavage planes for this phase correspond to the (110) planes, and although some evidence for this orientation was apparent, other orientations were also observed.

For bilayer films, a significant structural mismatch exists between the (010) surface of α-MoO_3 and most α-$NiMoO_4$ orientations. Misfit calculations for various orientations of α-MoO_3 and the $NiMoO_4$ phases are provided in Table 7. (110), (101), and (001) orientations of both α- and β-$NiMoO_4$ were considered for (100), (010), and (001)

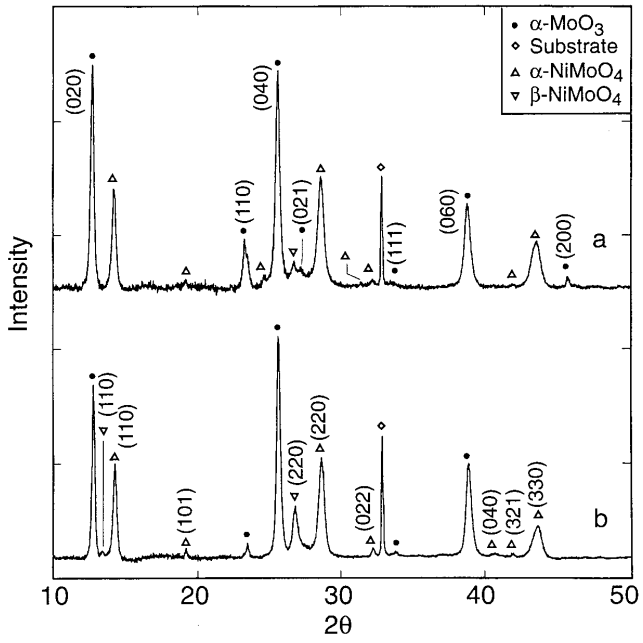

FIG. 8. XRD of (a) $NiMoO_4$ on (110)/(010) α-MoO_3 and (b) $NiMoO_4$ on (010) α-MoO_3.

orientations of α-MoO_3, although clearly formation of (010) α-MoO_3 dominated these studies. The misfit calculated for a (110) β-$NiMoO_4$–(010) α-MoO_3 interface was 5%; the corresponding misfit for the α-phase was nearly twice as large. The other orientations for β-$NiMoO_4$ on α-MoO_3 were much less favorable; this was true for all similar calculations for the α-phase. However, the presence of α-MoO_3 orientations other than (010) was observed for some bilayer films. In particular, peaks corresponding to (110), (021), and (111) planes were detected by XRD. For α-MoO_3, high index planes can be considered to be stepped surfaces or combinations of low index planes: for example the (110) plane of α-MoO_3 may be considered to be a combination of (101) terraces and (100) steps; the (021) plane may be regarded as a combination of (020) terraces and (001) steps (48). A low misfit (Table 7) was determined for (001) α-MoO_3 and (110) β-$NiMoO_4$ (1.3%): this may be responsible for the observation of (021) α-MoO_3 planes in the bilayer materials. Similarly, the misfits calculated for both the (001) and (100) planes of α-MoO_3 and (110) α-$NiMoO_4$ were

TABLE 7

Crystallographic Misfits between α-MoO_3 and α-$NiMoO_4$ or β-$NiMoO_4$

		Misfit %	
$NiMoO_4$ growth	α-MoO_3 orientation	α-$NiMoO_4$	β-$NiMoO_4$
(110)	(100)	3.4	12.8
	(010)	9.6	5.0
	(001)	3.6	1.3
(101)	(100)	17	14.5
	(010)	25	26
	(001)	22	20
(011)	(100)	10	21
	(010)	20	26
	(001)	15	27

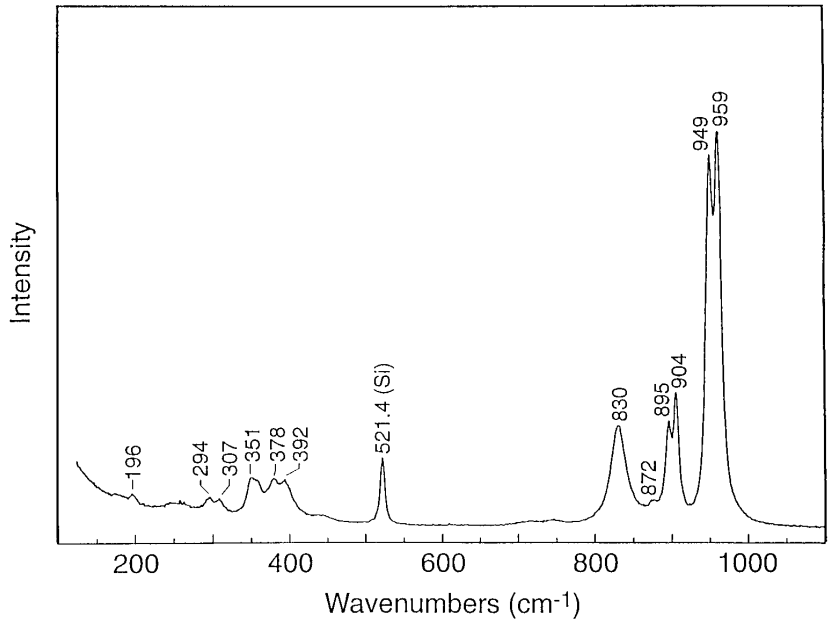

FIG. 9. Laser Raman spectrum of β-$NiMoO_4$ on Si at 450°C.

low. This may be responsible for the observation of (110) and (111) α-MoO_3 orientations, although this would imply that α-$NiMoO_4$ would be formed. Some indication of the presence of both $NiMoO_4$ phases at the interface was indeed provided by TEM (sample C). A possible mechanism for the formation of other orientations of α-MoO_3 during the deposition of $NiMoO_4$ would involve the deposition of some of the material as α-MoO_3. A consequence of this mechanism would be the existence of "excess Ni" (or a Ni oxide material) in the film (assuming no loss to the sputtering chamber environment). Another possible explanation for the presence of other orientations of α-MoO_3 would involve the reconstruction of the (010) surface.

Based on characterization by several techniques, an interfacial region of β-$NiMoO_4$ or a β-$NiMoO_4$-like material was formed. Direct evidence for the existence of a β-$NiMoO_4$-like material in this transition region was provided by LRS which was sensitive to the structural differences between α-$NiMoO_4$ and β-$NiMoO_4$. While both α-$NiMoO_4$ and β-$NiMoO_4$ have a monoclinic structure, α-$NiMoO_4$ consists of an octahedrally coordinated network of NiO_6 and MoO_6; β-$NiMoO_4$ involves NiO_6 octahedra and MoO_4 tetrahedra. α-$NiMoO_4$ has Mo-O stretching modes in the Raman spectrum at 706, 830 (weak), 914, and 960 cm^{-1}; β-$NiMoO_4$ has "pairs" of stretching modes at 949 and 960 cm^{-1} and 895 and 904 cm^{-1}, and the 830 cm^{-1} band is also more intense than that for α-$NiMoO_4$ (36). The clearest evidence for the β phase was provided for thin films of $NiMoO_4$ on (010) α-MoO_3 (samples C and D). There also was an indication of a structural transformation due to the increased halfwidth (FWHM) of the peak in the region of 959–961 cm^{-1} compared to single phase material. The intensity of peaks assigned to β-$NiMoO_4$ and the broadening of bands were less apparent as more material was deposited, presumably due to the subsequent formation of α-$NiMoO_4$.

Complementary information regarding the existence of β-$NiMoO_4$ at the interface was also provided by XRD, TEM, and SAD characterization. For thin films of $NiMoO_4$ on α-MoO_3, the XRD results confirmed the presence of β-$NiMoO_4$, although only one peak [corresponding to the (110) plane] could clearly be observed (another less intensive peak was apparent for some films). Misfit calculations (Table 7) are consistent with the observation of this orientation on (010) α-MoO_3. The relative intensity of the (110) β-$NiMoO_4$ peak decreased with the deposition of more material (α-$NiMoO_4$). TEM and SAD results tended to indicate formation of both α-$NiMoO_4$ and β-$NiMoO_4$. The microcrystalline structure of most regions of the $NiMoO_4$ films deposited at shorter times (sample C) was believed to be rather uniform; larger crystallines of single phase α-$NiMoO_4$ were observed only for longer deposition times. The orientation of this material also tended to be (110), which was consistent with misfit calculations (Table 7).

Previous studies of NiO–$NiMoO_4$ solutions have demonstrated that the β-phase can be stabilized by the presence of NiO. If "excess" NiO was formed in the films (or was deposited concurrently), there may have been an increased tendency to form β-$NiMoO_4$. This would reinforce the effects expected due to the comparatively good crystallographic match between β-$NiMoO_4$ and the (010) [or perhaps (001)] α-MoO_3 surface. The amount of NiO material may be very small at interface, and therefore characterization would be expected to be difficult. In addition, detection of this material by LRS and XRD is not readily achieved, as mentioned previously.

Previous investigations of $NiMoO_4$ and MoO_3 (in single-phase studies) have provided relevant information for the current study of multiphase catalysts. Catalytic studies of $NiMoO_4$ have suggested that: (1) Ni^{2+} sites are active for hydrocarbon activation in selective oxidation, (2) oxygen mobility in $NiMoO_4$ is low, and (3) the β phase has a higher intrinsic activity for dehydrogenation of propane to propene than the α phase (35, 49–53). The environments of the lattice oxygen are different for these phases since the α-$NiMoO_4$ phase consists of infinite chains of edge sharing NiO_6 and MoO_6 octahedra and the β-$NiMoO_4$ phase consists of NiO_6 octahedra and MoO_4 tetrahedra (49, 50, 54, 55). The differences in the catalytic selectivities of the α-$NiMoO_4$ and β-$NiMoO_4$ films determined in the studies reported here were small. β-$NiMoO_4$ appeared to have somewhat higher catalytic activity than α-$NiMoO_4$. This could be due to changes in surface morphology as the result of the preparation according to a phase transformation process (i.e., from α-$NiMoO_4$). The β-phase is also believed to be more difficult to reduce than the α-phase because of the tetrahedral oxygen coordination of Mo which consequently is less nucleophilic and less active for insertion (54). The β-phase may be more effective for hydrocarbon chemisorption and perhaps hydrogen abstraction (functions related to dehydrogenation); it may be less capable of inserting oxygen into hydrocarbon intermediate species. The differences in catalytic activity between α- and β-phases may be expected to be less significant for 1,3-butadiene oxidation than that for other reactions which have been examined, such as the dehydrogenation of propane (35) and the selective oxidation of 1-butene (33).

The catalytic activity of MoO_3 has been associated with the ability to insert lattice oxygen into the activated/adsorbed hydrocarbon species. The ability of MoO_3 to chemisorb and activate oxygen may be rather limited (20, 21). Formation of crystallographic shear (CS) structures may facilitate lattice oxygen insertion in a mechanism involving a dynamic surface with rapid lattice oxygen diffusion (56, 57) although the importance of these extended defects has been questioned recently (58). The catalytic properties of different MoO_3 crystal planes have been studied extensively: edge planes such as (100), (001), and (101)

are more active for hydrocarbon activation while the basal (010) plane is more easily reduced (leading to the formation of combustion products) (59, 61). Other reports have suggested that the bridging Mo–O–Mo sites on MoO_3 (010) surface are more nucleophilic than the terminal oxygen sites and are capable of inserting oxygen into the hydrocarbon molecules (21). The structure sensitivity of MoO_3 in selective oxidation has been questioned based on the difficulties in quantifying the results for relatively low-activity multigranular crystallites (62).

The sputtered catalysts—both single-phase and multiphase materials—generally had higher activities for 1,3-butadiene selective oxidation than did precipitated or impregnated materials. The conversion rate of 1,3-butadiene, as expressed on the basis of unit surface area of materials, was higher by at least an order of magnitude (30). At a low preparation temperature (400–500°C as compared to 800–1000°C for solid-state preparations), the materials probably retained more surface defects (steps, kinks) which may be important sites for hydrocarbon and oxygen activation. In addition to having more active sites, the nature of the sites (and consequently the reaction mechanism) may be different for sputtered catalysts: significantly higher yields of furan and 2(5*H*)-furanone were indeed observed (30).

Nevertheless, as for the precipitated or impregnated catalysts, an enhancement in catalytic activity and selectivity was observed for the multicomponent $NiMoO_4$–MoO_3, films, indicating a synergetic effect was involved. The bilayer materials produced larger amounts of furan, 2(5*H*)-furanone, and maleic anhydride compared to single-phase materials. Comparing the results for samples C and D, the conversion rate for sample D was nearly twice that of sample C, but the selectivities were very similar. The main difference between samples C and D was the amount of $NiMoO_4$ deposited on the α-MoO_3 (8 min for sample C vs 20 min for sample D): as stated previously, the role of $NiMoO_4$ layer may be to provide active sites for chemisorption and activation of hydrocarbon molecules. This has been suggested as the rate limiting step for the reaction of propylene oxidation in which the catalytic centers for adsorption of propylene molecules usually are transition-metal ion sites (44). Our results also indicated that the α-$NiMoO_4$ was active for furan, 2(5*H*)-furanone, and maleic anhydride formation, but the 1,3-butadiene conversion rate was relatively low. β-$NiMoO_4$ had higher conversion rates and comparable selectivity, as discussed previously. Some enhancement in selectivity for maleic anhydride and in the 1,3-butadiene conversion rate was observed also for the α-MoO_3-on-α-$NiMoO_4$ films (compared to the single-phase materials); however, the CO or CO_2 yields were high. Sputtered single-phase α-MoO_3 films had high rates of 1,3-butadiene conversion, but CO or CO_2 production was also larger. As stated, α-MoO_3 has been discussed as providing oxygen insertion sites for selective oxidation (57); complete oxidation sites (associated with Mo=O) are also believed to be present on the (010) surface (60). Thus, the (010) plane of α-MoO_3 may have two different types of catalytic properties: one for nucleophilic oxygen insertion and the other for complete oxidation. It may be expected that one function can be more effective than the other depending on the state of the hydrocarbon intermediate on the surface and the dynamic nature of the surface (e.g., reduction state). For bilayer materials, higher selectivity to partial oxidation products may also be attributed to a blocking of combustion sites on α-MoO_3 by the overlayer material, as has been suggested for precipitated catalysts (29, 30).

Some information affecting previously proposed models for multiphase catalysts mentioned frequently in the literature has been provided by our studies. Researchers have proposed that interfacial materials having a nonuniform composition—in this case a solid solution—can be the active phase for selective oxidation; epitaxial growth at an interface has also been suggested (11). In this study, formation of a "thermodynamically unstable" phase (β-$NiMoO_4$) has been observed at the interface, and some oriented growth for α- and β-$NiMoO_4$ on α-MoO_3 was observed. This may lead to the formation of new active sites, compared to pure α- and β-$NiMoO_4$ phases, and further characterization is being conducted to provide additional structural and compositional information at the interface. The present studies indicate that β-$NiMoO_4$ itself may perform somewhat better than α-$NiMoO_4$ for 1,3-butadiene oxidation. However, improvements in performance were also noted as more α-$NiMoO_4$ was deposited on the α-MoO_3. Much work in the literature has discussed another model for multicomponent catalysts involving a remote control mechanism: synergetic effects have been ascribed to surface diffusion of spillover oxygen species between separate phases ("contaminated" phases were to be avoided); nevertheless, the increase in conversion was believed to be accompanied by the creation of new active sites (21). The results reported in this study—in comparison to our previous work on precipitated or impregnated catalysts—indicated that formation of an interfacial material can occur for multiphase molybdate catalysts: this would clearly be expected for a preparation technique such as sputtering which likely ensures close contact between the phases. Previous models have also proposed that the existence of "coherent" boundaries can be beneficial by (1) modifying the metal-ion site configuration and (2) facilitating the transportation of oxygen species by lowering the potential barrier of charge transfer (5). These effects were considered mainly due to structural matches between phases rather than the results of "new" interfacial materials. Our results have shown that the increase of catalytic activity and selectivity was achieved despite some degree of apparent misfit between α-$NiMoO_4$ and the (010) α-MoO_3 surface. The presence of β-$NiMoO_4$ may be required to reduce the structural misfit for active and selective catalysts.

5. CONCLUSION

Single and multicomponent thin films of MoO_3 and $NiMoO_4$ were produced by reactive sputtering. Single component MoO_3 films were identified as α-MoO_3 with a strong basal (010) orientation and smooth surface morphology. Single component $NiMoO_4$ films were multicrystalline and exhibited the monoclinic structure of α-$NiMoO_4$ with no strongly preferred orientation. The bilayer $NiMoO_4$–MoO_3 films deposited by sputtering resulted in the formation of an additional interfacial region having a structure resembling β-$NiMoO_4$.

Synergetic effects for catalytic activity and selectivity have been observed for thin films of multicomponent $NiMoO_4$–MoO_3 which are similar to those for precipitated catalysts. The multilayer films provide active sites for hydrocarbon activation, hydrogen abstraction, and oxygen insertion in a manner similar to the single phase materials. However, the enhanced selectivities may indicate that new sites are formed, likely at the interface where an interfacial material exists. Improvements in selectivity may also be due to blockage of complete combustion sites.

ACKNOWLEDGMENTS

XPS characterization was performed by Jim Anderegg of the Ames Laboratory–USDOE. This work was sponsored by the Office of Basic Energy Sciences, Chemical Sciences Division, and was conducted through the Ames Laboratory which is operated for the U.S. Department of Energy by Iowa State University under Contract W-7405-ENG-82.

REFERENCES

1. Weng, L. T., and Delmon, B., *Appl. Catal. A* **81**, 141 (1992).
2. Grasselli, R. K., *React. Kinet. Catal. Lett.* **35**, 327 (1987).
3. Keulks, G. W., Krenzke, L. D., and Noterdam, T. M., *Adv. Catal.* **27**, 183 (1978).
4. Bordes, E., *in* "Structure–Activity and Selectivity Relationships in Heterogenous Catalysis" (R. K. Grasselli and A. W. Sleight, Eds.), p. 21. Elsevier, Amsterdam, 1991.
5. Courtine, P., *in* "Solid State Chemistry in Catalysis" (R. K. Grasselli and J. F. Brazdil, Eds.), p. 37. ACS,Washington, DC, 1985.
6. Vejux, A., and Courtine, P., *J. Solid State Chem.* **63**, 179 (1986).
7. Bordes, E., and Courtine, P., *J. Catal.* **57**, 236 (1979).
8. Vejux, A., and Courtine, P., *J. Solid State Chem.* **23**, 93 (1978).
9. Bordes, E., and Courtine, P., *J. Catal.* **57**, 236 (1979).
10. Jung, J. S., Bordes, E., and Courtine, P., *in* "Adsorption and Catalysis on Oxide Surfaces" (M. Che and G. C. Bond, Eds.), p. 345. Elsevier, Amsterdam, 1985.
11. Brazdil, J. F., Glaeser, L. C., and Grasselli, R. K., *J. Phys. Chem.* **87**, 5485 (1983).
12. Brazdil, J. F., Teller, R. G., Grasselli, R. K., and Kostiner, E., *in* "Solid State Chemistry in Catalysis" (R. K. Grasselli and J. F. Brazdil, Eds.), p. 57. ACS, Washington, DC, 1985.
13. Glaeser, L. C., Brazdil, J. F., Hazzle, M. A., Mehicic, M., and Grasselli, R. K., *J. Chem. Soc. Faraday Trans. 1* **81**, 2903 (1985).
14. Grasselli, R. K., *Appl. Catal.* **15**, 127 (1985).
15. Teller, R. G., Antonio, M. R., Brazdil,, J. F., and Grasselli, R. K., *J. Solid State Chem.* **64**, 249 (1986).
16. Grasselli, R. K., Centi, G., and Trifiro, F., *Appl.Catal.* **57**, 149 (1990).
17. Dicosimo, R., Burrington, J. D., and Grasselli, R. K., *J. Catal.* **102**, 234 (1986).
18. Bruckman, K., Haber, J., and Wiltowski, T., *J. Catal.* **106**, 188 (1987).
19. Bruckman, K., Grabowski, G., Haber, J., Mazurkiewicz, A., Sloczynski, J., and Wiltowski, T., *J. Catal.* **104**, 71 (1987).
20. Haber, J., *in* "New Developments in Selective Oxidation by Heterogeneous Catalysis" (P. Ruiz and B. Delmon, Eds.), p. 279. Elsevier, Amsterdam, 1992.
21. Haber, J., and Serwicka, E. M., *React. Kinet. Catal. Lett.* **35**, 369 (1987).
22. Cadus, L. E., Xiong, Y. L., Gotor, F. J., Acosta, D., Naud, J., Ruiz, P., and Delmon, B., *in* "New Developments in Selective Oxidation II" (V. Cortes Corberan and S. Bellon, Eds.), p. 41. Elsevier, Amsterdam, 1994.
23. Weng, L. T., Ruiz, P., and Delmon, B., *in* "New Developments in Selective Oxidation by Heterogeneous Catalysis" (P. Ruiz and B. Delmon, Eds.), p. 339. Elsevier, Amsterdam, 1992.
24. Weng, L. T., Ruiz, P., Delmon, B., and Duprez, D., *J. Mol. Catal.* **52**, 349 (1989).
25. Zhou, B., Ceckiewicz, S., and Delmon, B., *J. Phys. Chem.* **91**, 5061 (1987).
26. Weng, L. T., Ma, S. Y., Ruiz, P., and Delmon, B., *J.Mol. Catal.* **61**, 99 (1990).
27. Weng, L. T., Patrono, P., Sham, E., Ruiz, P., and Delmon, B., *in* "New Developments in Selective Oxidation" (G. Centi and F. Trifiro, Eds.), p. 120. Elsevier, Amsterdam, 1990.
28. Ozkan, U., and Schrader, G. L., *J. Catal.* **95**, 126 (1985).
29. Ozkan, U., and Schrader, G. L., *J. Catal.* **95**, 137 (1985).
30. Ozkan, U., and Schrader, G. L., *J. Catal.* **95**, 147 (1985).
31. Ozkan, U., Smith, M. R., and Driscoll, S. A., *in* "New Developments in Selective Oxidation by Heterogeneous Catalysis" (P. Ruiz and B. Delmon, Eds.), p. 363. Elsevier, Amsterdam, 1992.
32. Ozkan, U. S., Gill, R. C., and Smith, M. R., *Appl. Catal.* **62**, 105 (1990).
33. Zou, J. Y., and Schrader, G. L., *in* "New Developments in Selective Oxidation II" (V. Cortes Corberan and S. Bellon, Eds.), p. 19. Elsevier, Amsterdam, 1994.
34. Zou, J. Y., and Schrader, G. L., *Thin Solid Films,* submitted for publication.
35. Renzo, F. D., Mazzocchia, C., Thomas, G., and Vernay, A. M., *Reactivity Solids* **6**, 145 (1988).
36. Mazzocchia, C., Renzo, F. D., Aboumirad, C., and Thomas, G., *Solid State Ionics* **32/33**, 228 (1989).
37. Lu, H. C., Ph.D thesis, Iowa State University, 1992.
38. de Boer, D. K. G., and van den Hoogenhof, W. W., *in* "Advances in X-ray Analysis" (C. S. Barrett *et al.,*Eds.), p. 35. Plenum, New York, 1991.
39. Lashier, M. E., and Schrader, G. L., *J. Catal.* **128**, 113 (1991).
40. JCPDS 35-0609, *Natl. Bur. Stand. Monogr. (US)* **25**, 20 118 (1984).
41. Spevack, P. A., and McIntyre, N. S., *J. Phys. Chem.* **96**, 9029 (1992).
42. JCPDS 33-0948, *Natl. Bur. Stand. Monogr. (US)* **25**, 1962 (1982).
43. Dufrense, P., Payen, E., Grimblot, J., and Bonnelle, J. P., *J. Phys. Chem.* **85**, 2344 (1981).
44. Kim, K. S., and Davis, R. E., *J. Elect. Spec.* **1**, 251 (1972).
45. Mazzocchia, C., Renzo, F. D., Aboumirad, C., and Thomas, G., "Proc. Congr. Phys. Chem.," p. 289. Societa di Fisica Chimica Italiana, Siena, 1986.
46. JCPDS 44-1159, 1992.
47. Grimblot, J., Payen, E., and Bonnelle, J. P., "Proc. 4th Int. Conf. Chem. Uses Molybdenum" (H. F. Barry, P. C. Mitchell, Eds.), p. 261. Climax Molybdenum Co.,Golden, CO, 1983.
48. Abon, M., Mingot, B., Massardier, J., and Volta, J. C., *in* "Structure–Activity Relationships in Heterogeneous Catalysis" (R. K. Grasselli and A. W. Sleight, Eds.), p. 67. Elsevier, Amsterdam, 1991.
49. Mazzocchia, C., Aboumrad, C., Diagne, C., Tempesti, E., Herrmann, J. M., and Thomas, G., *Catal. Lett.* **10**, 181 (1991).

50. Mazzocchia, C., DiRenzo, F., Centola, P., and Rosso, R. D., "Proc. 4th Int. Conf. Chem. Uses Molybdenum" (H. F. Barry, P. C. Mitchell, Eds.), p. 406. Climax Molybdenum Co.,Golden, CO, 1983.
51. Wolfs, M. W., and Batist, P. A., *J. Catal.* **32**, 25 (1974).
52. Smith, G. W., and Ibers, J. A., *Acta. Cryst.* **19**, 269 (1965).
53. Courtine, P., Cord, P. P., Pannier, G., Dumas, J. C., and Montarnal, R., *Bull. Soc. Chim. France,* **12**, 4816 (1968).
54. Brito, J., Barbosa, A., Albornoz, A., Severino, F., and Laine, J., *Catal. Lett.* **26**, 329 (1994).
55. Haber, J., *in* "Solid State Chemistry in Catalysis" (R. K. Grasselli and J. F. Brazdil, Eds.), p. 3. ACS, Washington, DC, 1985.
56. Haber, J., *Kinet. Catal.* **21**, 123 (1980).
57. Haber, J., *Pure Appl. Chem.* **50**, 923 (1978).
58. Gai-Boyes, P. L., *Catal. Rev.-Sci. Eng.* **34** (1 and 2), 1 (1992).
59. Volta, J. C., *Appl. Catal.* **18**, 1 (1985).
60. Ziokowski, J., *J. Catal.* **80**, 263 (1983).
61. Abon, M., Massardier, J., Mingot, B., Volta, J. C., Floquet, N., and Bertrand, O., *J. Catal.* **134**, 542 (1992).
62. Oyama, S. T., *Bull. Chem. Soc. Jpn.* **61**, 2585 (1988).